Journal of Marine Science and Application (2025) 24: 947-958
https://doi.org/10.1007/s11804-024-00466-7

RESEARCH ARTICLE

Experimental and Computational Studies on a Cylinder with Continuous and Discrete Strakes

Subramanian Sarvalogapathi[1], Kumar Narendran[1] and Rajamanickam Panneer Selvam[1]

Received: 10 May 2024 / Accepted: 11 August 2024

Abstract

Cylindrical cross sections are critical components in offshore structures, including jacket platform legs, pipelines, mooring lines, and risers. These cylindrical structures are subjected to vortex-induced vibrations (VIV) due to strong ocean currents, where vortices generated during fluid flow result in significant vibrations in crossflow and in-flow directions. Such vibrations can lead to severe damage to platforms, cables, and riser systems. Consequently, mitigating VIV caused by vortex-induced forces is important. This study investigates the hydrodynamic performance of five strake models relative to a bare cylinder at moderate Reynolds numbers. The models encompass one conventional continuous helical strake (HS) and four helical discrete strake (HDS) with varying segment spacing between the fins. The hydrodynamic performance, specifically lift and drag force coefficients, was computed using a Reynolds averaged Navier–Stokes-based CFD solver and validated with experimental measurements. The conventional HS suppresses 95% of the lift force but increases the drag force by up to a maximum of 48% in measurements. The HDS suppress the lift force by 70%–88% and increase the drag force by 15%–30%, which is less than the increase observed with the HS. Flow visualization showed that HS and HDS cylinders mitigate vortex-induced forces by altering the vortex-shedding pattern along the length of the cylinder. The HDS achieves a reduction in drag compared with the conventional continuous HS. The segment spacing is found to significantly impact the reduction in vortex-induced forces.

Keywords CFD; Continuous helical strakes; Drag force measurements; Helical discrete strakes; RMS lift force coefficient; Segment spacing; Strouhal number; Vortex-induced forces

1 Introduction

The oil and gas industries rely heavily on offshore platforms, such as jacket platforms, tension-leg platforms, etc. The cross-sectional geometry for most offshore systems is cylindrical due to their symmetrical shapes and high moment of inertia that aid in withstanding environmental loads. These structures, when subjected to ocean currents, develop a distinctive flow pattern known as von Kármán vortex street (Halse, 1997; Jhingran, 2008; Sarpkaya, 1979; Sumer and Fredsoe, 1997). The vortices are shed downstream (wake side) of the cylinder, which leads to oscillatory hydrodynamic forces called vortex-induced forces. These forces cause the structure to vibrate, which is termed vortex-induced vibration (VIV). Several studies (Bearman, 1984; King, 1977; Sarpkaya, 2004, 1979; Williamson and Govardhan, 2004) on various aspects of VIV are available. In VIV, the oscillating frequency of vortices aligns with the natural frequency of the structure, which is a phenomenon termed "lock-in" (Lee et al., 2014; Vandiver and Marcollo, 2004; Williamson and Govardhan, 2004; Zahour, 2016). The lock-in phenomenon is associated with the resonance condition, which causes large oscillations that lead to structural failures (Narendran et al., 2015; Sarpkaya, 1979; Williamson and Govardhan, 2004). This phenomenon exists in numerous applications, including electrical transmission lines, chimney towers, heat exchanger tubes, nuclear fuel rods, and oil and gas industries. Thus, researchers have attempted to minimize vortex-induced forces using flow control strategies. The flow control strategies are classified

Article Highlights

- The HDS configuration consist of smaller fins arranged helically around the cylinder at equal distance along its length. Four different segment spacings (S/D) are examined in this numerical and experimental study.
- Both HS and HDS cylinders mitigate vortex-induced forces by disrupting the vortex shedding pattern along the cylinder's length.
- It was observed that HDS cylinders achieved a reduction in RMS lift coefficient with less drag compared to HS cylinders.
- The segment spacing (S/D) was found to have a significant impact on reducing vortex-induced forces.

✉ Subramanian Sarvalogapathi
sarvalogam1991@gmail.com

[1] Department of Ocean Engineering, Indian Institute of Technology Madras, Chennai 600036, India

as active and passive devices. The control systems in active devices effectively reduce vortex-induced forces across a wide range of flow regimes. However, due to the difficulties involved with the former technology, such as additional investment (CAPEX and OPEX) and unfavorable power input-to-output ratio, these active devices are seldom recommended. Passive flow control devices are relatively economical devices, which are becoming the most appropriate, feasible, and affordable solution for offshore industries. Several studies explore the overall effectiveness of passive suppression (flow control) devices.

The aerodynamic and hydrodynamic performances of passive suppression devices in cylinders, including near wake stabilizers, surface protrusions, and shrouds, were reviewed by Zdravkovich (1981) under the categories of omnidirectional and unidirectional devices. More recent studies have shown that ventilated trousers, which are measured for omnidirectional flow control, are effective devices (Assi et al., 2022; Assi and Crespi, 2019; Korkischko and Meneghini, 2011; Kumar et al., 2018). Given that the directionality of ocean currents is an important concern in the field, omnidirectional devices (Helical strake (HS)) are preferable. HS is one of the effective devices used extensively for mitigating VIV and vortex-induced forces. Numerous authors (Franzini et al., 2009; Gaczek and Kawecki, 1996; Korkischko et al., 2007; Korkischko and Meneghini, 2011; Pinto et al., 2007) have extensively examined and discussed the design of HS parameters, including pitch, strake height, and single, double, and triple start strakes.

Scruton and Flint (1964) developed an HS using a sharp-edged rectangular section wrapped around the cylinder in a three-start helical form to mitigate VIV. The experiments were carried out in cylinders with and without HS (three starts) by Korkischko et al. (2007) and Korkischko and Meneghini (2010). Various parameters were investigated, including pitch (P = 5D, 10D, 15D), strake height (h = 0.1D, 0.2D, 0.25D), mass ratio, and damping, where D is the diameter of the cylinder. The experimental studies were performed in Re ranging from 2 000 to 10 000 for P = 10D and h = 0.2D. They reported that the HS suppresses VIV effectively by preventing the shear layer interaction near the base region of the cylinder body. The motivation of the study is derived from the HS type of passive flow control device, which is continuous for the entire length of the cylinder. Although a number of investigations related to HS type are available, the focus of the authors shifted toward investigating discrete strakes positioned helically along the length of the cylinder. The use of this type may eventually reduce material costs and become economically feasible compared with the HS type. To the best of the authors' knowledge, helical discrete strake (HDS) have been used in chimney towers but not yet in offshore structures.

The authors believed that numerical studies complemented with experimental data would be beneficial in investigating the performance of HDS with respect to bare cylinder (BC) and HS cylinders. There are a number of numerical studies were available to investigate the hydrodynamic effects in two-dimensional and three-dimensional forms (Fu and Wan, 2017; Fu et al., 2023). However, the number of works exploring HS and HDS is limited. According to the limited studies available (Carmo et al., 2012; Constantinides and Oakley, 2006), the suppression of vortex-induced forces for a cylinder with HS is due to the disruption of the correlation of shedding patterns along the length of the cylinder. In addition, offshore applications of HS cylinders effectively reduce lift forces and displacement at the expense of a substantial drag force due to their increased height (h > 0.1D) and projected area. Therefore, drag force must be mitigated through a proper design of low-drag devices.

Many flow control devices, such as splitter plates, guiding vanes, and fairings, are available on the market to suppress the VIV effects of cylinders known as near wake stabilizers. They have been shown to be much more effective in unidirectional flows than in multidirectional flows. Discrete strakes were utilized in steel and concrete chimneys to reduce VIV (IS 4998 (Part 1), 1992). Novak (1968) proposed arranging rectangular fins in a single start helical pattern around a stack to minimize oscillations. According to IS 4998 (Part 1)(1992), the three-start discrete strakes were designed as helixes at the top of the chimney to avoid resonance due to VIV. Rao (1988) reported that discrete strakes were used in over 20 chimneys and had a lower drag penalty with respect to conventional HS. Assi et al. (2022) and Assi and Crespi (2019) designed a type of discrete strake known as bladed strakes (BS) and twisted bladed strake (TBS) over the cylinder with pitch (P) = 5D and strake height (h) = 0.2D. In terms of drag reduction, BS and TBS were both effective VIV suppressors. Li et al. (2020) applied discrete strakes to the lab-scaled riser model with an aspect ratio of 111.11 and varied the strake parameters, such as segment spacing and various helical patterns. The performance of discrete helical strake was investigated using numerical and experimental methods at Re ranging from 4 500 to 10 800. Discrete Double- and triple-start helical strakes were more effective in VIV suppression, with the best efficiency achieved at a discrete spacing of 0.52D. The discrete spacing, strake height, helical pitch, and number of helical forms, along with other design parameters of discrete helical strake, influence the VIV suppression. Different HDS have not been widely investigated by researchers. Thus, a comprehensive analysis of the HS, HDS, and BC is necessary to measure and compute the hydrodynamic performance in a uniform current flow.

This study aims to elaborate and estimate the hydrodynamic performances of BC, HS, and HDS for various segment spacings between the fins in order to suppress vortex-induced forces using a commercial CFD solver for two dif-

ferent orders of *Re*, i.e., O(10^3) and O(10^4). This study is supported by an in-house experiment conducted to validate the numerical method over a similar range of *Re*, i.e., at *Re* = 4 612 and 5 814. Studies on HS are available in measurements and computations with *Re* = 5 000 (Korkischko and Meneghini, 2011). Therefore, the authors performed studies at *Re* in that range and were curious to understand the hydrodynamic performance of HS and HDS cases at *Re* in the range of O(10^4). In this study, the numerical investigations were conducted at *Re* = 5 000 and *Re* = 10 000.

The rest of the manuscript is structured as follows. The design and development of the HS and HDS cylinders are presented in Section 2. The numerical methodology includes the governing equation, computational domain, and mesh details, which are shown in Section 3. The test facility and experimental setup are outlined in Section 4. Section 5 discusses the validation studies and the effect of strakes on vortex-induced forces, including force coefficients and flow visualization around the cylinder. A summary and conclusion of the present study are included in Section 6.

2 Design and development of discrete and continuous strakes

The strake height (*h*), pitch (*P*), and number of helixes are important parameters for efficiently suppressing vortex-induced forces. Korkischko et al. (2007) and Korkischko and Meneghini (2010) found that a conventional three-start HS with a 10*D* pitch and 0.2*D* strake height worked well for mitigating vortex-induced forces. Therefore, similar configurations are used in the present study. The core diameter of all cylinder models is *D* = 40 mm, and the length is *L* = 10*D*. Figure 1 shows the CAD model of BC, HS, and HDS with varying segment spacings. The geometrical parameters for the strakes are listed in Table 1. The discrete strakes used in this study could be envisioned as discontinuous HS, with smaller fins helically wrapped around the cylinder with equal spacing along its span, as shown in Figures 1(c)–(f). In the current study, the segment spaces (*S*/*D*) considered are 0.25 (HDS-1), 0.5 (HDS-2), 0.75 (HDS-3), and 1 (HDS-4). The fin width (*W* = 0.15*D*) is kept constant for all cases, as presented in Table 1. The segment spacing (*S*) between the fins is shown in Figure 2.

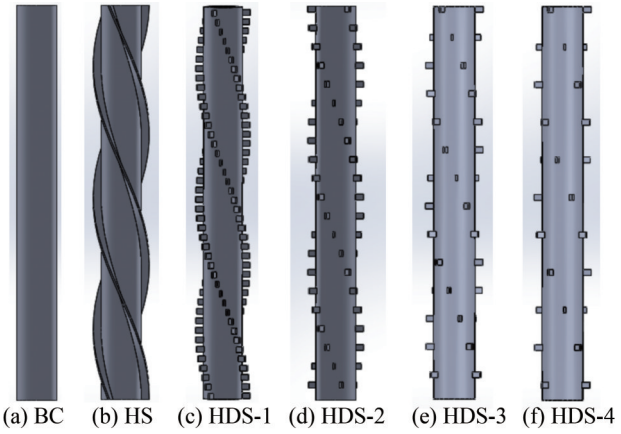

Figure 1 CAD models of passive flow control devices

Table 1 Design parameters of BC, HS, and HDS (*L*/*D* = 10)

Parameters/ Cylinder cases	BC	HS	HDS-1	HDS-2	HDS-3	HDS-4
Height of strake (*h*/*D*)	–	0.2	0.2	0.2	0.2	0.2
Pitch (*P*/*D*)	–	10	10	10	10	10
Spacing between fins (*S*/*D*)	–	–	0.25	0.5	0.75	1

BC: Bare cylinder; HS: Cylinder with continuous helical strake; HDS: Cylinder with helical discrete strake

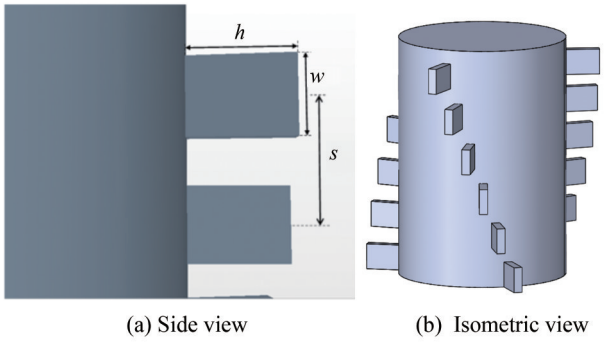

Figure 2 Details of the HDS model

3 Numerical methodology

3.1 Governing equations

The continuity and momentum equations, which govern the flow field for this study, are a Newtonian incompressible fluid. The Reynolds averaged Navier–Stokes (RANS) equation with the shear stress transport (SST) $k-\omega$ turbulence model developed by Menter (1994) is as follows:

$$\frac{\partial U_i}{\partial x_i} = 0 \tag{1}$$

$$\frac{\partial u_i}{\partial t} + \frac{\partial u_i u_j}{\partial x_j} = -\frac{1}{\rho}\frac{\partial p}{\partial x_i} + \frac{\partial}{\partial x_j}\left[\left(\nu + \nu_t\right)\frac{\partial U_i}{\partial x_j}\right] \tag{2}$$

where ρ and p are the fluid density and pressure, respectively; ν is the kinematic viscosity; and ν_t is the turbulent viscosity.

3.2 Computational domain and boundary conditions

The computational domain is fixed in terms of cylinder diameter (D) to form a cuboid of length, breadth, and height as $40D \times 20D \times 10D$ in (X, Y, Z) directions, as shown in Figure 3, along with appropriate boundary conditions. The cylinder is positioned at $10D$ from the inlet, $30D$ from the outlet, and $10D$ from the top, bottom, and side walls to mitigate the wall effects. For all simulations, the length of the cylinder is $10D$, and it consists of one pitch of helical strakes ($10D$). The boundary condition of the upstream side is defined as velocity inlet, the pressure outlet is on the downstream side, and the cylinder is the wall with no-slip condition implemented. The closing surfaces of the cylinder are defined as walls with slip conditions, while the top and bottom surfaces are assigned symmetry conditions.

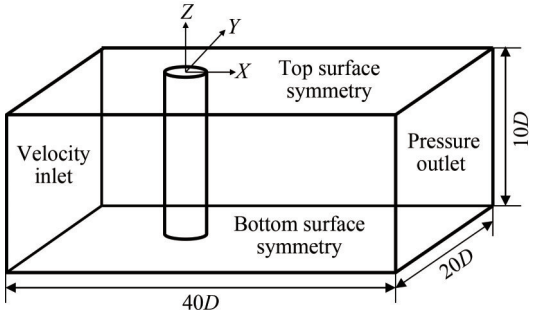

Figure 3 Computational domain with boundary conditions

The computational domain is discretized using trimmer mesh strategies, which creates the volume mesh by cutting the hexahedral mesh with the geometry surface. It has user-defined controls to generate the refined mesh in the wake region. The strakes near the cylinder required a finer mesh to capture flow separation and vortices. In this study, a trimmed hexahedral mesh is used to create the volume mesh, as illustrated in Figures 4 and 5. The prism layers are used to capture the viscous effects on the body wall. The thickness of the first wall layer (Δy) of the boundary layer is computed using Eq. (3) (Xu and Zhu, 2009).

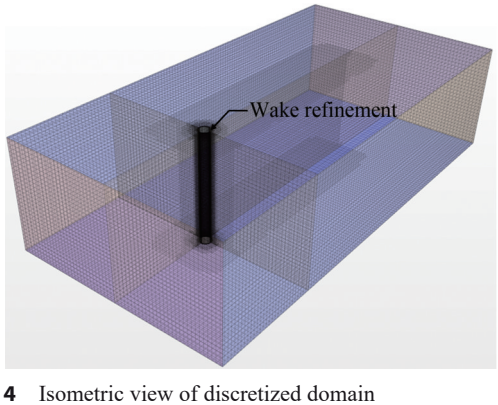

Figure 4 Isometric view of discretized domain

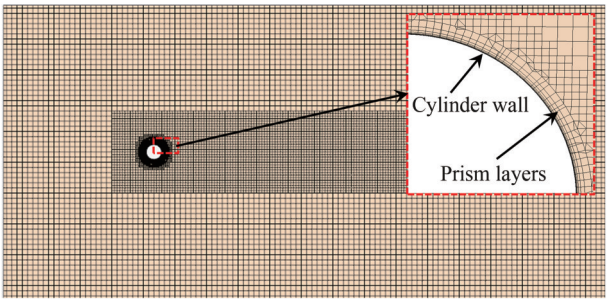

Figure 5 Cross section view of discretized grid and boundary layers at the cylinder wall

$$y^{+} = 0.172 Re^{0.9} \frac{\Delta y}{D} \tag{3}$$

where y^{+} is a wall function and is kept as <1 for all simulation cases.

The numerical model and solver settings implemented for simulations are three-dimensional with an unsteady, implicit, segregated solver. The model is simulated using the RANS technique with the SST $k-\omega$ turbulence model to account for turbulence effects. The SST $k-\omega$ model is a combined model that employs $k-\omega$ near the cylinder wall and $k-\omega$ away from the wall, and it is best suited for the flow separation problem (Younoussi and Ettaouil, 2024).

3.3 Grid convergence study

The CFD simulations are approximate solutions, and discretization error is one of the most significant errors affecting the accuracy of solutions, resulting in uncertainty. The grid convergence index (GCI) is used in this study to assess the numerical uncertainty caused by discretization errors. The GCI is calculated using the method proposed by Celik et al. (2008). Three meshes with varying refinements are considered for this study. The Strouhal number (St) and mean drag force coefficient $\left(\overline{C_D}\right)$ are chosen as the performance parameters, and the grid refinement factor is set to greater than 1.3, as recommended in the literature. The GCI calculation results are shown in Table 2. If the GCI value across consecutive grids is less than 1%, then the grid has reached spatial convergence, and further refinement will not affect the solution. The medium grid is used for further calculations in this study.

4 Experimental methodology

Experiments are conducted in the glass flume at the Department of Ocean Engineering, IIT Madras, which is 22 m long, 0.6 m wide, and 0.8 m deep. The side walls and bottom of the flume are made of glass to facilitate flow visibility. The current flow is generated by the 30 HP centrifugal pump, which is controlled by a variable frequency

Table 2 Grid convergence index based on Celik et al. (2008)

Parameters		Values
Description	Symbols	
Number of cells (10^6)	N1, N2, N3	5.15, 1.85, 0.67
Grid refinement factor	r_{21}, r_{32}	1.404, 1.404
Performance parameter (St)	φ_1, φ_2, φ_3	0.212 4, 0.204 9, 0.204 1
Performance parameter ($\overline{C_D}$)	φ_1, φ_2, φ_3	1.204, 1.160, 1.149
Apparent order	p	6.51
Approximate relative error (%)	e_a^{21}, e_a^{32}	3.52, 0.4
Extrapolated values	φ_{ext}^{12}, φ_{ext}^{32}	0.213 3, 0.205
Extrapolated relative error (%)	φ_{ext}^{21}, φ_{ext}^{32}	0.43, 0.05
GCI (%)	GCI_{fine}^{21}, GCI_{medium}^{32}	0.54, 0.06

drive that varies the flow velocity from the inlet. Figure 6 shows a schematic layout of the plan view (a) and elevation view (b) of the glass flume with the arrangement of the test model. The studies include the investigation of six different cylinder types (BC, HS, HDS-1, HDS-2, HDS-3, and HDS-4) for two different *Re* values of 4 612 and 5 814.

Figure 7 presents the experimental setup with the test model (cylinder), which is fixed using aluminum frames. The frames are placed exactly on the edges of the glass flume wall and are fixed using a nut and bolt arrangement to provide stability and weight transfer. A single-component beam-type load cell is designed and fabricated to measure the hydrodynamic force in the inline flow direction (drag force) at the upper end of the cylinder. The load cell is coupled to the PMX data acquisition system, which records drag forces by means of voltage. The cylinder is placed in the center of the flume to reduce wall effects. The smallest distance is applied at the bottom of the cylinder to transfer loads to the load cell at the top with a blockage ratio of 0.03%.

The test model cylinders are fabricated in-house using FDM 3D printing technology, as shown in Figure 8. The geometrical parameters are shown in Table 1. The calibration constant of the load cell is estimated to be 48.068 N/(mV/V) using a standard calibration procedure.

The capability range of generating flow current velocity is limited due to the limitations of the glass flume facility. Therefore, the possible *Re* values that can be achieved are 4 612 and 5 814. Moreover, $\overline{C_D}$ is reported to be constant for *Re*, which ranges from 10^3 to 10^6 (Korkischko and Meneghini, 2011) and also found to be nearly constant in

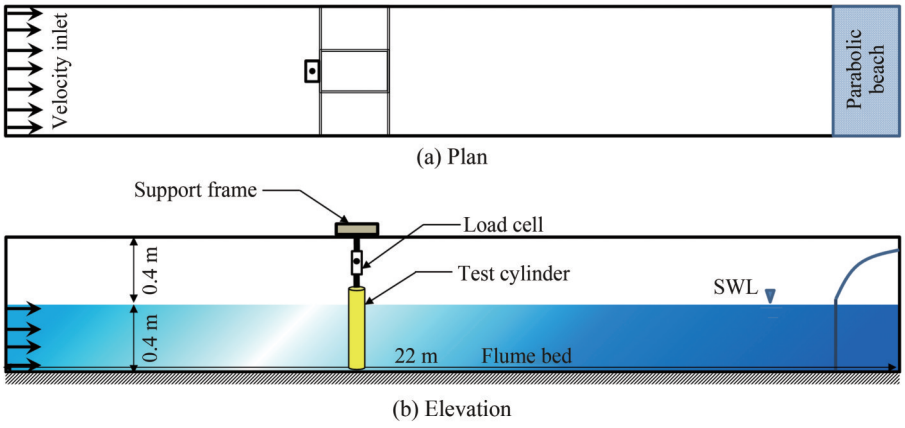

Figure 6 Glass flume with model setup

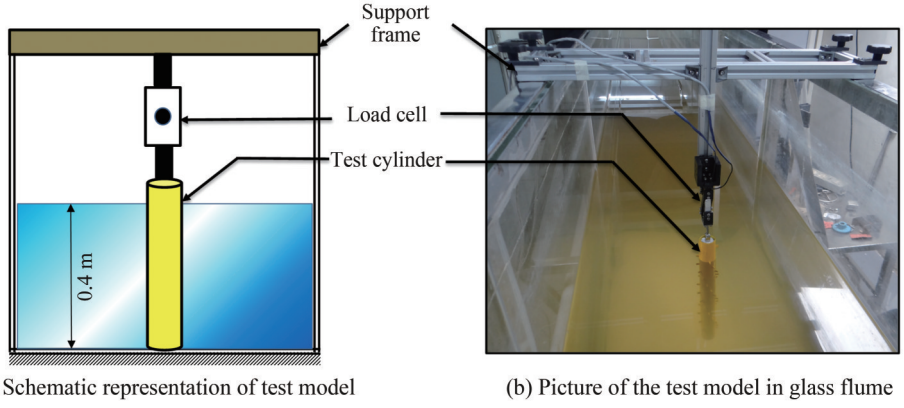

Figure 7 Sectional view of model setup

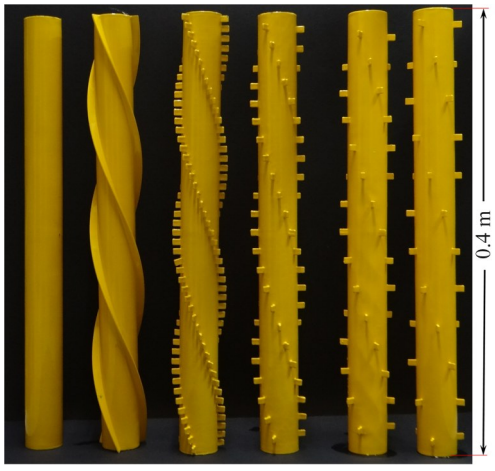

Figure 8 3D printed cylinder models

the measured *Re* range from *Re* = 1500 to *Re* = 5 100. Therefore, the measurements complement numerical results in the present studies if the *Re* lies in the same order. Based on the flow regimes, *Re* = 4 612 and *Re* = 5 814 are selected for the present experimental studies to validate the case studies from the numerical model at *Re* = 5 000.

5 Results and discussion

The hydrodynamic forces are resolved into lift force (F_l) and drag force (F_d), which are represented as lift force coefficient (C_L) and drag force coefficient (C_D). These coefficients are evaluated using Eqs. (4) and (5), respectively.

$$C_D = \frac{F_d}{\frac{1}{2}\rho U^2 DL} \tag{4}$$

$$C_L = \frac{F_l}{\frac{1}{2}\rho U^2 DL} \tag{5}$$

The Strouhal number (*St*) is given by Eq. (6), and it represents the non-dimensional shedding frequency, which is the ratio of the product of vortex-shedding frequency (f_v) and the diameter of the cylinder to the flow velocity (U).

$$St = \frac{f_v D}{U} \tag{6}$$

The parameters are tabulated in Table 3.

$\widehat{C_L}$ and $\overline{C_D}$ are defined as the root mean square (RMS) of the lift force coefficient and mean drag force coefficient, respectively, as shown in Eqs. (7) and (8).

$$\overline{C_D} = \frac{\sum C_D}{n} \tag{7}$$

Table 3 Description of parameters in Eqs. (4)–(6)

Symbol	Description	Unit
F_l	Lift force	N
F_d	Drag force	N
ρ	Density of fluid	kg/m^3
U	Free stream velocity	m/s
D	Diameter of cylinder	m
L	Length of cylinder	m
f_v	Vortex-shedding frequency	Hz

$$\widehat{C_L} = \sqrt{\frac{1}{n}\sum C_L^2} \tag{8}$$

where *n* represents the number of samples.

They are estimated from the numerical time histories of lift and drag force coefficients, as shown in Figure 9. The Strouhal number computed from the frequency spectrum of the lift force coefficient is 0.205, as shown in Figure 10, which is aligned with the literature (Sumer and Fredsoe, 1997). The time history of drag force obtained from experiments and numerical simulation is converted into drag force coefficient using Eq. (4). Similarly, the time history of lift force is converted into lift force coefficient using Eq. (5). The $\overline{C_D}$ for a particular *Re* is calculated using Eq. (7). The average of lift force coefficient is zero. Thus, the RMS of lift force coefficient used for quantifying the lift force is calculated using Eq. (8).

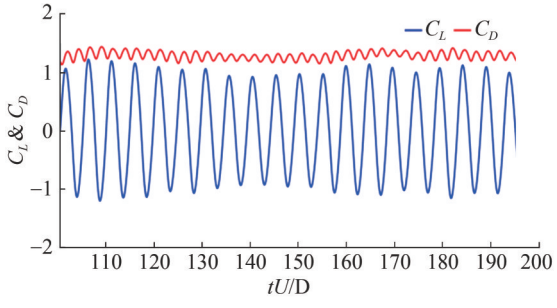

Figure 9 Time history of lift and drag force coefficients for BC at *Re* = 5 000

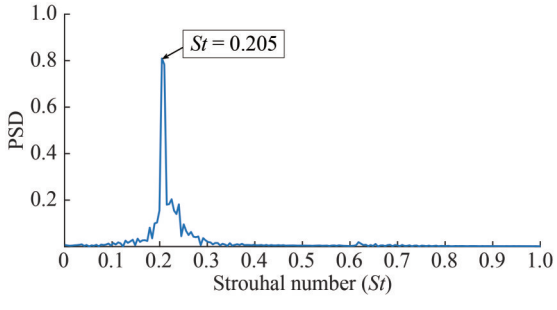

Figure 10 PSD of lift force coefficient for BC at *Re* = 5 000

5.1 Validation comparisons of experimental and numerical prediction results

Preliminary tests are performed on the BC and the HS cylinder to ensure that the test setup is correct and to validate the present results with earlier investigations. Similarly, hydrodynamic forces for the BC and HS cases are computed at Re = 5 000 to verify the present numerical study. The results are tabulated in Table 4. $\overline{C_D}$ is considered the reference value to compare the results of the present numerical and experimental study with those of earlier investigations.

Table 4 Mean drag force coefficient ($\overline{C_D}$) for BC and HS

Cases	Re	$\overline{C_D}$	
		BC	HS
Korkischko and Meneghini (2011)	1 500–5 100	1.16	1.59
Experiment	4 612	1.029	1.53
Experiment	5 814	1.126	1.55
Numerical	5 000	1.16	1.43

Korkischko and Meneghini (2011) reported that the $\overline{C_D}$ value for the BC is 1.16 at Re = 1 500 to Re = 5 100. This value is close to the present measurements (Re = 4 612 and Re = 5 814) and numerical computations (Re = 5 000), as tabulated in Table 4. The measured and computed values of $\overline{C_D}$ are observed to have a satisfactory match with the values present in the literature. Experiments and numerical analysis show that the mean drag force for the HS case increases by around 48% when compared with the BC due to increased area of projection (Korkischko and Meneghini, 2011).

5.2 Drag force analysis

The hydrodynamic $\overline{C_D}$ values on the cylinder models are compared and presented in Figures 11 and 12. Figure 11 exhibits the results of the BC, HS, and HDS models at various spacings for Re of 4 612, 5 000, and 5 814. Similar observations are made at Re = 10 000, as shown in Figure 12.

As shown in Figure 11, the $\overline{C_D}$ value on the HS model is higher by 36% than that on the BC case, with a $\overline{C_D}$ value computed as 1.43 using numerical simulations and measured as 1.55 from experiments. The deviation between these values is approximately 7%. An average increase of 36% with respect to the BC is attributed to the increased projected area due to the presence of HS along the length of the cylinder. As shown in Figure 11, a substantial decrease in the $\overline{C_D}$ values is observed for all HDS cases considered in this study when compared with the HS case. This reduction is associated with the vortex shedding pattern along the length of the cylinder, which is discussed in detail in Section 5.3. The $\overline{C_D}$ value of HDS-1 is reduced by approximately 18% compared with that of the HS case, as per experimental measurement. However, the segment spacing between the fins is 0.25D, which is smaller and more like that of an HS cylinder. This smaller spacing leads to a higher projected area and results in a mean drag coefficient that aligns closely with the HS case during numerical approximation. It shows a slight increase of less than 7% in numerical simulation at Re = 5 000. The measured and computed $\overline{C_D}$ values for HDS-2 show an 18% decrease with respect to that for the HS case. The HDS-3 model experiences a decrease in $\overline{C_D}$ of approximately 27%, which is close to that of the BC. For the HDS-4 model, the $\overline{C_D}$ value decreases by approximately 15% but differs from numerical and experimental findings. This difference might be due to the turbulence or scale effects.

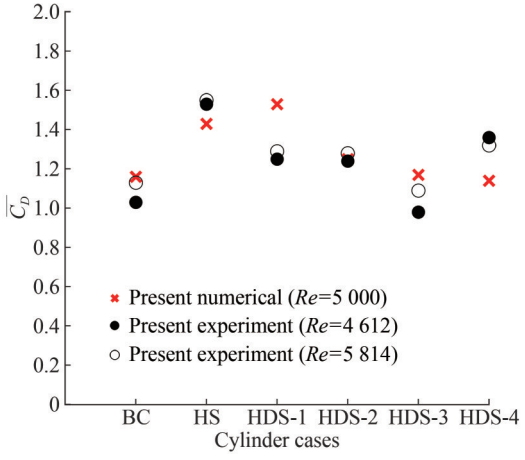

Figure 11 Mean drag force coefficient ($\overline{C_D}$) for all cylinder cases at Re = 5 000, Re = 4 612, and Re = 5 814

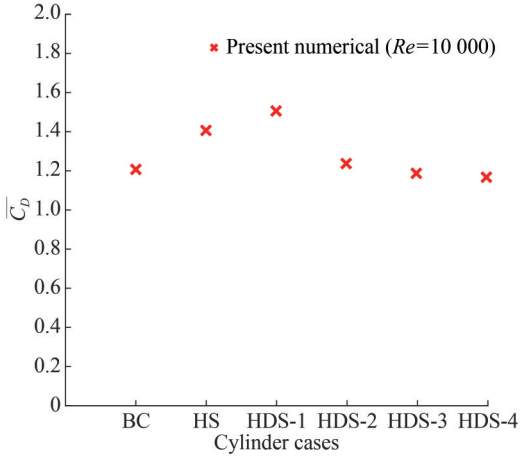

Figure 12 Mean drag force coefficient ($\overline{C_D}$) for all cylinder cases at Re = 10 000

Figure 12 displays the numerical $\overline{C_D}$ values for each cylinder model at Re = 10 000. The $\overline{C_D}$ value increases by 17% for the HS case compared with BC and by 7% higher for the HDS-1 compared with HS due to smaller segment space similar to the observations in Re = 5 000. The HDS-2,

HDS-3, and HDS-4 cylinders achieve a 15% reduction in $\overline{C_D}$ compared with the HS cylinder.

5.3 Lift force analysis

The hydrodynamic $\widehat{C_L}$ for each cylinder model is calculated numerically and is shown in Figures 13 and 14 for Re = 5 000 and Re = 10 000, respectively. The $\widehat{C_L}$ value of straked cylinders are compared with that of BC. The HS results in a reduction in $\widehat{C_L}$ of up to 97% with respect to BC, while HDS cylinders show a decrease of $\widehat{C_L}$ by about 80%–90% compared with BC at Re = 5 000. Korkischko and Meneghini (2010) highlighted that the height of strakes has a profound influence on lift forces and control of the shear layer separation, which is elaborated in Section 5.3. A similar pattern is observed in $\widehat{C_L}$ at Re = 10 000; the HS cylinder achieves a maximum reduction of 95% in $\widehat{C_L}$, whereas HDS cylinders exhibit reductions ranging from approximately 70% to 88% when compared with BC. The HDS cylinders reduce the $\widehat{C_L}$ value with minimal drag penalty, as observed in Figures 11–14.

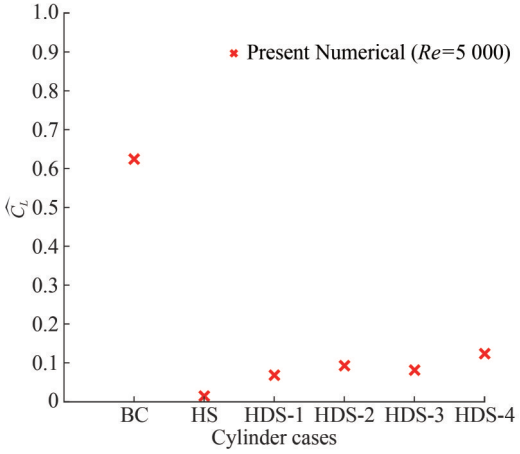

Figure 13 RMS lift force coefficient $(\widehat{C_L})$ for cylinder cases at Re = 5 000

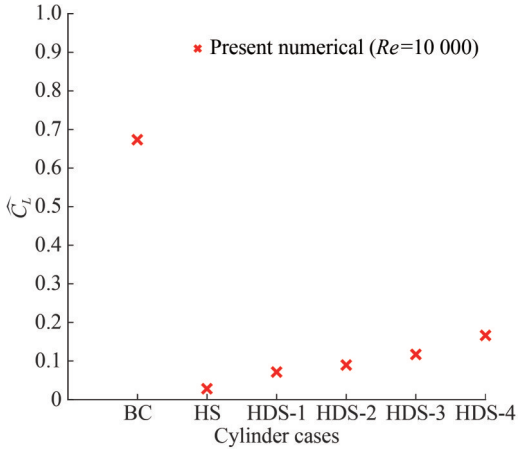

Figure 14 RMS lift force coefficient $(\widehat{C_L})$ for cylinder cases at Re = 10 000

5.4 Flow visualization around the cylinder

The flow dynamics play an important role in understanding the influence of hydrodynamic forces on the cylinders in the cases of HS and HDS. The flow dynamics exhibit the nature of vortex-shedding patterns along the length of the cylinder. Figures 15(a)–(f) and Figures 16(a)–(f) present the pictures of flow profiles in two different views obtained using computational studies for Re = 5 000 at non-dimensional time (tu/D) = 196. Figures 15(a)–(f) present the snapshots of instantaneous vorticity contours obtained in the XZ-plane view at the mid-section of the cylinder for all the cases considered in this study. Similarly, Figures 16(a)–(f) show an isometric view of the vortex-shedding pattern along the length of the cylinder at three different sections: near the top, middle, and bottom. The vortex-shedding patterns are compared in the three sections to investigate the uniformity of the vortex-shedding patterns along the length of the cylinder with HS and HDS cases.

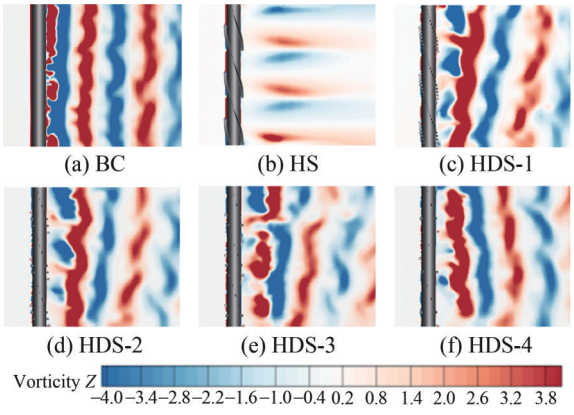

Figure 15 Instantaneous vorticity contour for all cylinders Re = 5 000 at $\left\{\frac{tu}{D}\right\}$ = 196 XZ-plane view at the mid-section of the cylinder

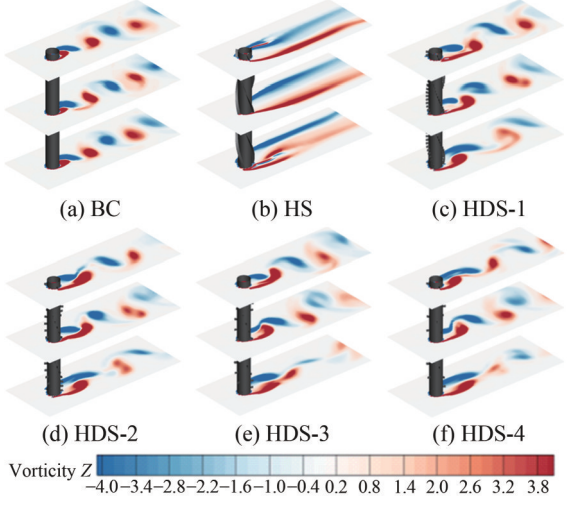

Figure 16 Instantaneous vorticity contour for all cylinder Re = 5 000 at $\left\{\frac{tu}{D}\right\}$ = 196 isometric view at the three different sections (middle, top, and bottom end of the cylinder)

The shedding pattern at the wake side of the BC is observed to be continuous and undistorted, as shown in Figure 15(a). For the HS and HDS cases, the vortex-shedding pattern is distorted along the length of the cylinder, as shown in Figures 15(b)–(f). The distortion of vortices is observed to be profound for the HDS cases, namely, HDS-1, HDS-2, HDS-3, and HDS-4 (Figures 15(c)–(f)), compared with the HS case. Among the HDS cases, the flow pattern of HDS-3 is unique in the aspects of strong distortion and breakup of the vortices compared with other HDS cases. This observation can be associated with the reduction in mean drag forces, as shown in Figure 11, which is supported by experimental measurements. Although the distortion is profound for HDS cases, the drag forces for HDS-1, HDS-2, and HDS-4 are higher by 5%–30% with respect to HDS-3.

The distortion is more complex along the length of the cylinder, as presented in Figures 16(a)–(f). Complexity in-flow patterns is clearly observed in the figures presented for three different sections. Figure 16(a) presents the BC case, where the vortex-shedding pattern is regular along the length of the cylinder. The flow profile is uniform even for the HS case, as shown in Figure 16(b). For HDS-1, as shown in Figure 16(c), the vortices that are shed at the ends (top and bottom) of the cylinder are completely different from the mid-section of the cylinder. Even the patterns are different at each end. As observed closely in Figure 16(c) (HDS-1), the positive vorticity vector (red color) at the top end of the cylinder is elongated slightly compared with the mid-section and bottom end of the cylinder. Similar observations can be made in the other HDS cases, as shown in Figures 16(d)–(f). In other words, the vortex formation length varies along the length of the cylinder, which influences the vortex-induced forces. However, the vortex formation length is not discussed in this study.

The pressure contour plots also provide additional insights into the understanding of the drag force coefficients for various cases. The pressure coefficient (C_p) contour plots for all the cases considered in this study are presented in Figures 17(a)–(f). A significant difference in the pressure coefficient values is observed in the wake side of the cylinder with HS, as shown in Figure 17(b), compared with the wake side of the BC, as shown in Figure 17(a). The size of the contour with a negative C_p value (−1) is smaller for the BC case than for the HS case, which might influence the drag force coefficient. The size of the C_p contours or the intensity of the C_p values is reduced for HDS-1 compared with that for the HS case, but it is still higher than that for the BC case. This result is due to the segment spacing between fins for HDS-1, which is smaller and might emulate a continuous HS. With a further increase in the segment space, the size of the pressure contours also reduces, which reaches the lowest drag force coefficient value for HDS-3, as shown in Figure 17(e).

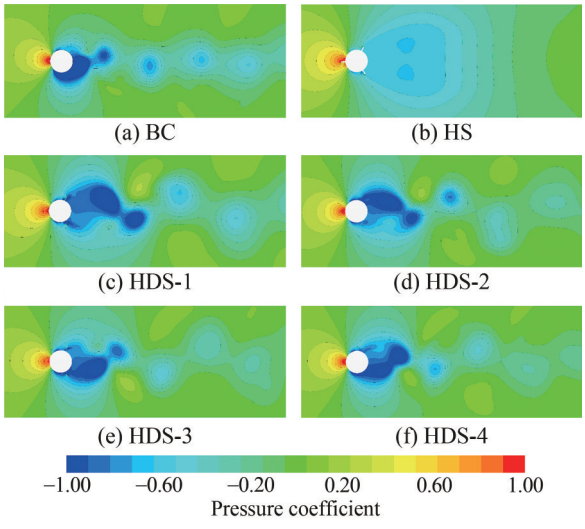

Figure 17 Instantaneous pressure coefficient for all cylinders Re = 5 000 at $\left\{\frac{tu}{D}\right\}$ = 196 XY-plane view at the mid-section of the cylinder

Similarly, the vorticity contours around the cylinder for Re = 10 000 are depicted in Figures 18(a)–(f) and Figures 19(a)–(f) from two different perspectives at a nondimensional time (tu/D) = 392. As previously observed for Re = 5 000, the shedding pattern on the wake side of the BC is undistorted. Meanwhile, it is distorted for the HS and HDS cases along the length of the cylinder, as shown in Figures 18(a)–(f) for Re = 10 000. The distortion of vortices in the HDS cases correlates with a reduction in mean drag forces, which is approximately 17% lower than those in the HS case. Figures 19(a)–(f) provides an isometric view of the vortex-shedding pattern along the length of the cylinder at three different sections. Differences in shedding patterns exist among all cylinder cases near the wake zone. The presence of strakes causes variations in flow separation at each section, which affects the vortex formation length along the cylinder. This variation influences the vortex-induced forces, specifically in the HDS cases, as illustrated in Figures 19(c)–(f).

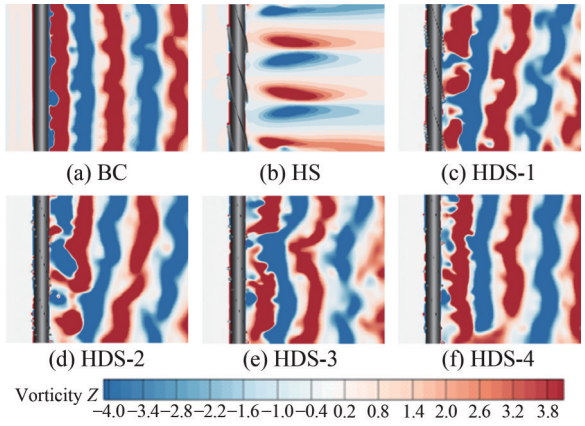

Figure 18 Instantaneous vorticity contour for all cylinders Re = 10 000 at $\left\{\frac{tu}{D}\right\}$ = 392 XZ-plane view at the mid-section of the cylinder

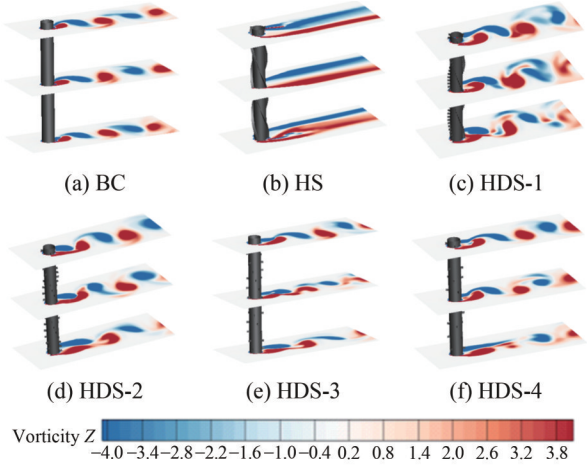

Figure 19 Instantaneous vorticity contour for all cylinders Re = 10 000 at $\left\{\frac{tu}{D}\right\}$ = 392 isometric view at the three different sections (middle, top, and bottom end of the cylinder)

The pressure coefficient (C_p) contour plots for all cylinder cases at Re = 10 000 are shown in Figures 20(a)–(f). As observed for Re = 5 000, a similar pattern is evident at Re = 10 000, displaying significant differences in the pressure coefficient. The size of the negative region is larger on the wake side of the HS case than that of other cylinder cases, such as BC and HDS, which results in an increased drag coefficient. The segment spacing of the strakes in the HDS cases significantly influences the pressure coefficient, which leads to a smaller negative C_p region than that in the HS case.

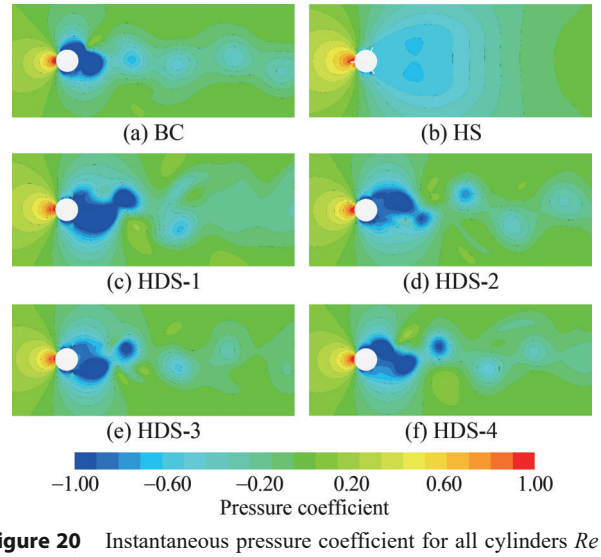

Figure 20 Instantaneous pressure coefficient for all cylinders Re = 10 000 at $\left\{\frac{tu}{D}\right\}$ = 392 XY-plane view at the mid-section of the cylinder

6 Conclusions

In this study, RANS simulations were conducted to investigate the effectiveness of HDS against a BC and a cylinder with continuous HS in suppressing vortex-induced forces. Experiments were also conducted to measure the drag forces on BC, HS, and HDS cylinders. The key findings are obtained as follows:

1) The HDS models reduce drag force by 18%–35%, with maximum reductions for segment spacings of S/D = 0.5 and S/D = 0.75. They also decrease lift force by 70%–88%. Overall, the HDS performance in the reduction of vortex-induced forces is satisfactory.

2) In the HDS models, the vortices shed at the ends of the cylinder differ significantly from those at the mid-section. The presence of discrete strakes distorts the vortex formation length along the cylinder, which leads to a reduction in vortex-induced forces.

3) All cylinder models with strakes disrupt the vortex-shedding pattern, which effectively suppresses vortex-induced forces. In particular, the segment spacing (S/D) in the HDS model significantly contributes to this reduction, as evidenced by experimental measurements and computational studies.

HDS is effective in mitigating vortex-induced forces in current flows for offshore structural systems such as SPAR platforms and risers. Future research incorporating inline and crossflow displacements of HDS cylinders will provide valuable insights to further enhance the efficacy of HDS in offshore environments.

Nomenclature

BC	Bare cylinder
BS	Bladed strake
C_D	Drag force coefficient
$\overline{C_D}$	Mean drag force coefficient
CFD	Computational fluid dynamics
C_L	Lift force coefficient
$\widetilde{C_L}$	RMS lift force coefficient
C_p	Pressure coefficient
D	Diameter of the cylinder
DAQ	Data acquisition system
F_d	Drag force
FDM	Fused deposition modeling
F_l	Lift force
f_v	Vortex-shedding frequency
GCI	Grid convergence index
h	Height of strake
HDS	Helical discrete strake
HS	Helical continuous strake
L	Length of cylinder
ρ	Density of fluid
PSD	Power spectral density

RANS	Reynolds averaged Naiver–Stokes
S	Segment spacing between strakes
SST	Shear stress transport
St	Strouhal number
TBS	Twisted bladed strake
U	Free stream velocity
VFD	Variable frequency drive
VI	Vortex induced
VIV	Vortex-induced vibration
W	Width of discrete strake

Acknowledgement The authors are thankful to the Department of Ocean Engineering, Indian Institute of Technology Madras, Tamil Nadu, India, for providing facilities for experimental studies. The authors are grateful to the HPCE and IIT Madras for providing computational resources to conduct numerical studies. The authors also express their gratitude to M/s Seaconvoy Systems Engineering Private Limited, Chennai, India, for their support in the fabrication of models and experimental setup.

Competing interest The authors have no competing interests to declare that are relevant to the content of this article.

References

Assi GRS, Crespi T (2019) Laboratory investigation of helical strakes with serrated and twisted fins to suppress VIV. Proceedings of the ASME 2019 38th International Conference on Ocean, Offshore and Arctic Engineering, Glasgow, V002T08A019. https://doi.org/10.1115/OMAE2019-95129

Assi GRS, Crespi T, Gharib M (2022) Novel geometries of serrated helical strakes to suppress vortex-induced vibrations and reduce drag. Appl. Ocean Res. 120: 103034. https://doi.org/10.1016/j.apor.2021.103034

Bearman PW (1984) Vortex shedding from oscillating bluff bodies. Annu. Rev. Fluid Mech. 16: 195-222. https://doi.org/10.1146/annurev.fl.16.010184.001211

Carmo BS, Gioria RS, Korkischko I, Freire CM, Meneghini JR (2012) Two- and three-dimensional simulations of the flow around a cylinder fitted with strakes. Proceedings of the ASME 2012 31st International Conference on Ocean, Offshore and Arctic Engineering, Rio de Janeiro, Brazil, 781-790. https://doi.org/10.1115/OMAE2012-83603

Celik IB, Ghia U, Roache PJ, Freitas CJ, Coleman H, Raad PE (2008) Procedure for estimation and reporting of uncertainty due to discretization in CFD applications. J. Fluids Eng. Trans. ASME 130(7): 0780011. https://doi.org/10.1115/1.2960953

Constantinides Y, Oakley OH (2006) Numerical prediction of bare and straked cylinder VIV. Proceedings of the 25th International Conference on Offshore Mechanics and Arctic Engineering, Hamburg, Germany, 745-753. https://doi.org/10.1115/OMAE2006-92334

Franzini GR, Fujarra ALC, Meneghini JR, Korkischko I, Franciss R (2009) Experimental investigation of vortex-induced vibration on rigid, smooth and inclined cylinders. J. Fluids Struct. 25(4): 742-750. https://doi.org/10.1016/j.jfluidstructs.2009.01.003

Fu B, Wan D (2017) Numerical study of vibrations of a vertical tension riser excited at the top end. J. Ocean Eng. Sci. 2(4): 268-278. https://doi.org/10.1016/j.joes.2017.09.001

Fu X, Fu S, Han Z, Niu Z, Zhang M, Zhao B (2023) Numerical simulations of 2-DOF vortex-induced vibration of a circular cylinder in two and three dimensions: A comparison study. J. Ocean Eng. Sci. https://doi.org/10.1016/j.joes.2023.08.006

Gaczek M, Kawecki J (1996) Analysis of cross-wind response of steel chimneys with spoilers. J. Wind Eng. Ind. Aerodyn. 65(1-3): 87-96. https://doi.org/10.1016/S0167-6105(97)00025-1

Halse KH (1997) On vortex shedding and prediction of vortex-induced vibrations of circular cylinders. PhD thesis, Norwegian University of Science and Technology, Trondheim

IS 4998 (Part 1) (1992) Criteria for design of reinforced concrete chimneys. Bureau of Indian standard, India, 1-12

Jhingran VG (2008) Drag amplification and fatigue damage in vortex-induced vibrations. MIT Libraries. Available from https://dspace.mit.edu/handle/1721.1/44804 [Accessed on March 26, 2024]

King R (1977) A review of vortex shedding research and its application. Ocean Eng. 4(3): 141-171. https://doi.org/10.1016/0029-8018(77)90002-6

Korkischko I, Meneghini JR (2010) Experimental investigation of flow-induced vibration on isolated and tandem circular cylinders fitted with strakes. J. Fluids Struct. 26(4): 611-625. https://doi.org/10.1016/j.jfluidstructs.2010.03.001

Korkischko I, Meneghini JR (2011) Volumetric reconstruction of the mean flow around circular cylinders fitted with strakes. Exp. Fluids 51: 1109-1122. https://doi.org/10.1007/s00348-011-1127-x

Korkischko I, Meneghini JR, Gioria RS, Jabardo PJ, Casaprima E, Franciss R (2007) An experimental investigation of the flow around straked cylinders. Proceedings of the ASME 2007 26th International Conference on Offshore Mechanics and Arctic Engineering, San Diego, USA, 641-647. https://doi.org/10.1115/OMAE2007-29057

Kumar N, Kumar Varma Kolahalam V, Kantharaj M, Manda S (2018) Suppression of vortex-induced vibrations using flexible shrouding—An experimental study. J. Fluids Struct. 81: 479-491. https://doi.org/10.1016/j.jfluidstructs.2018.04.018

Lee AH, Campbell RL, Hambric SA (2014) Coupled delayed-detached-eddy simulation and structural vibration of a self-oscillating cylinder due to vortex-shedding. J. Fluids Struct. 48: 216-234. https://doi.org/10.1016/j.jfluidstructs.2014.02.019

Li P, Liu L, Dong Z, Wang F, Guo H (2020) Investigation on the spoiler vibration suppression mechanism of discrete helical strakes of deep-sea riser undergoing vortex-induced vibration. Int. J. Mech. Sci. 172: 105410. https://doi.org/10.1016/j.ijmecsci.2019.105410

Menter FR (1994) Two-equation eddy-viscosity turbulence models for engineering applications. AIAA J. 32: 1598-1605. https://doi.org/10.2514/3.12149

Narendran K, Murali K, Sundar V (2015) Vortex-induced vibrations of elastically mounted circular cylinder at Re of the O(10^5). J. Fluids Struct. 54: 503-521. https://doi.org/10.1016/j.jfluidstructs.2014.12.006

Novak M (1966) The wind induced lateral vibration of circular guyed masts, tower-shaped steel and reinforced concrete structures. Symp. Int. Ass. Shell Struct., Bratislava

Pinto A, Broglia R, Ciappi E, Di Mascio A, Campana EF, Rocco P (2007) Vortex suppression efficiency of discontinuous helicoidal fins. Proceedings of the ASME 2007 26th International Conference on Offshore Mechanics and Arctic Engineering, San Dieg, USA, 813-820. https://doi.org/10.1115/OMAE2007-29255

Rao GNV (1988) A survey of wind engineering studies in India.

Sadhana 12: 201-218. https://doi.org/10.1007/BF02745665
Sarpkaya T (1979) Vortex-induced oscillations: A selective review. J. Appl. Mech. 46: 241-258. https://doi.org/10.1115/1.3424537
Sarpkaya T (2004) A critical review of the intrinsic nature of vortex-induced vibrations. J. Fluids Struct. 19: 389-447. https://doi.org/10.1016/j.jfluidstructs.2004.02.005
Scruton C, Flint AR (1964) Wind-excited oscillations of structures. Proc. Inst. Civ. Eng. 27: 673-702. https://doi.org/10.1680/iicep.1964.10179
Sumer M, Fredsoe J (1997) Hydrodynamics around cylindrical structures. World Scientific. https://doi.org/10.1142/62488
Vandiver JK, Marcollo H (2004) High mode number VIV experiments. Fluid Mech. its Appl. 75: 211-231. https://doi.org/10.1007/978-94-007-0995-9_15
Williamson CHK, Govardhan R (2004) Vortex-induced vibrations. Annu. Rev. Fluid Mech. 36: 413-455. https://doi. org/10.1146/annurev.fluid.36.050802.122128
Xu JL, Zhu, RQ (2009) Numerical simulation of VIV for an elastic cylinder mounted on the spring supports with low mass-ratio. J. Mar. Sci. Appl. 8: 237-245. https://doi. org/10.1007/s11804-009-8117-x
Younoussi S, Ettaouil A (2024) Calibration method of the $k-\omega$ SST turbulence model for wind turbine performance prediction near stall condition. Heliyon 10(1): e24048. https://doi.org/10.1016/j.heliyon.2024.e24048
Zahour A (2016) Helical strakes on High Mast Lighting Towers and their effect on vortex shedding lock-in. Master thesis, Purdue University, Indiana
Zdravkovich MM (1981) Review and classification of various aerodynamic and hydrodynamic means for suppressing vortex shedding. J. Wind Eng. Ind. Aerodyn. 7: 145-189. https://doi.org/10.1016/0167-6105(81)90036-2